

Assessment of DKIST/VTF Capabilities for the Detection of Local Acoustic Source Wavefronts

Corinne Morrell^{1,2,*}, Mark P. Rast^{1,2}, Shah Mohammad Bahauddin^{1,4}, and Ivan Milić³

¹ *Laboratory for Atmospheric and Space Physics, University of Colorado, Boulder, CO 80303, USA*

² *Department of Astrophysical and Planetary Sciences, University of Colorado, Boulder, CO 80309, USA*

³ *Institut für Sonnenphysik, Freiburg im Breisgau, Germany*

⁴ *Center for Astronomy, Space Science and Astrophysics, Independent University Bangladesh, Dhaka, Bangladesh*

Correspondence*:

Corinne Morrell

corinne.morrell@colorado.edu

ABSTRACT

Recent studies have demonstrated that temporal filtering can successfully identify local-acoustic-source wavefronts in radiative magnetohydrodynamic simulations of the solar photosphere. Extending this capability to observations promises new insight into the stochastic excitation of solar p-modes, the source depth distribution below the photosphere, and the dominant physical processes underlying acoustic wave excitation. Such measurements would also enable improved characterization of the complex wavefield in the lower chromosphere and open the possibility of ultra-local helioseismic diagnostics. In this work, we assess an observational strategy for the detection of local acoustic wavefronts on the Sun using the National Science Foundation's Daniel K. Inouye Solar Telescope's Visible Tunable Filter (DKIST/VTF). Because wavefront identification requires high spatial and temporal resolution and is limited by the small amplitudes of the wave perturbations, we focus on identifying specific wavelength combinations within spectral lines that maximize the sensitivity to the wave signal at the atmospheric heights where that signal is highest while minimizing contamination by atmospheric variability at other heights. Under the cadence and spectral resolution constraints of DKIST/VTF observations and for the particular simulated wavefront we examine, this approach suggests two possible strategies for the detection of acoustic wavefronts in solar observations: fast monochromatic imaging at 6302.425 Å, or ordered interleaved observations in the blue wing of either the Fe I 6302.5 Å or Fe I 5250.6 Å line (between 6302.419 Å and 6302.465 Å, or between 5250.579 Å and 5250.607 Å respectively).

Keywords: Solar oscillations, Wave propagation, Forward modeling, Imaging spectroscopy, High-cadence observations, Helioseismology

1 INTRODUCTION

There are two broad classes of stellar oscillations: high amplitude pulsations and low amplitude oscillations. Self-excitation by overstability is thought to account for the former in stars such as classical Cephieds, RR Lyrae stars, δ Scuti variables, and pulsating white dwarfs, among others (Cox, 2002; Aerts et al., 2010;

Daszyńska-Daszkiewicz, 2015; Samadi et al., 2015). By contrast, low-amplitude oscillations are typically associated with pulsationally stable stars, such as the Sun. Solar acoustic oscillations (*p*-modes) have radial velocity amplitudes in the photosphere of less than $10 - 20 \text{ cm s}^{-1}$ with associated intensity fluctuations of a few parts per million (e.g., Christensen-Dalsgaard, 2002). No known mechanism can limit overstable pulsational modes to such low amplitudes, and so continuous stochastic excitation is thought to sustain these oscillations (Goldreich and Keeley, 1977).

Differing theoretical treatments emphasize the importance of different aspects of the underlying compressible turbulence to stochastic excitation. Convective motions may transfer energy into the acoustic wave spectrum via Reynolds stresses (e.g., Lighthill, 1952, 1954; Stein, 1967; Goldreich and Keeley, 1977; Goldreich and Kumar, 1990; Balmforth, 1992; Kitiashvili et al., 2019), entropy fluctuations, (e.g., Stein and Nordlund, 1991; Goldreich et al., 1994; Rast, 1997; Nordlund and Stein, 1998; Rast, 1999; Samadi and Goupil, 2001; Samadi et al., 2001), or some combination of the two. More than one mechanism may be important, with the phase relationships between them reflecting the evolution of solar granulation (Rast, 1999). In particular, both modeling (e.g., Skartlien et al., 2000; Lindsey and Rempel, 2020) and observational (Rimmele et al., 1995; Goode et al., 1998; Strous et al., 2000; Roth et al., 2010; Bello González et al., 2010; Lindsey and Donea, 2013) evidence suggests that acoustic excitation on the Sun occurs preferentially in granular downflow lanes and is associated with strong impulsive downflow events. These may occur as a result of new downflow formation during granule fragmentation (Rast et al., 1993; Rast, 1995) or by the rapid enhancement of existing downflows. Acoustic emission in both cases includes dynamically-induced entropy fluctuations and Reynolds stresses (Stein and Nordlund, 1991; Goldreich et al., 1994; Rast, 1997; Nordlund and Stein, 1998; Rast, 1999; Samadi and Goupil, 2001; Samadi et al., 2001). In the case of granule fragmentation, the role of entropy fluctuations is enhanced by strong localized cooling (Rast, 1997, 1999). While uncertainties remain, due to the possible presence of a correlated noise component in the spectra (Roxburgh and Vorontsov, 1997; Nigam et al., 1998, but see Philidet et al. 2020), these excitation mechanisms are broadly consistent with constraints inferred from phase-difference spectra. In particular, the measured velocity–intensity phase relationships agree with the acoustic spectral signatures expected from rapidly forming downflow plumes (Skartlien and Rast, 2000; Severino et al., 2001). Other possible mechanisms for global *p*-mode excitation include solar flares, which can trigger transient acoustic waves (Kosovichev and Zharkova, 1998; Ambastha et al., 2003; Donea and Lindsey, 2005; Martínez et al., 2020; Lindsey et al., 2020), with coupling to solar *p*-modes somewhat uncertain but plausible (Lindsey et al., 2014; Hansen et al., 2016).

Thus, multiple acoustic excitation mechanisms may be active on the Sun and in other stars. Observational access to individual source events would allow for greater constraints to be placed on the source depth distributions, temporal phasing of the thermodynamic and dynamic fluctuations associated with the sources, and the coupling efficiencies to the global eigenmodes. Linking the observed wave field to specific generation sites would clarify distinct excitation pathways and their relative contributions, enable improved characterization of the complex wavefield propagating upward from the photosphere into the lower chromosphere, and open the possibility of ultra-local helioseismic diagnostics based on the local wave field emitted by the discrete sources.

1.1 The aim of this paper

In previous work, we have developed a diagnostic differencing scheme designed to isolate the small-amplitude acoustic perturbations generated by localized excitation events (Bahauddin and Rast, 2021, 2023), and have applied the method to numerical simulations to aid in the interpretation of early DKIST

observations of transient wave phenomena (Bahauddin et al., 2024). The method allows identification of coherent wavefronts by leveraging the difference between the timescales of granulation evolution and that of wavefront passage across the spatial grid. It was formulated and validated using a three-dimensional numerical simulation of quiet-sun granulation (Rempel, 2014), operating directly on the temperature, pressure, and velocity fields computed by the magnetohydrodynamic simulation. The reliability of the differencing scheme thus, at face value, depends critically on having access to one or more of these physical quantities with high fidelity, and direct application to observations would require inferring the three-dimensional thermodynamic structure of the solar atmosphere from spectroscopic or spectropolarimetric measurements through inversion codes (e.g., Del Toro Iniesta and Ruiz Cobo, 1996; del Toro Iniesta and Ruiz Cobo, 2016). In practice, however, this direct approach is limited by photon noise, finite spectral, spatial, and temporal resolution, radiative transfer degeneracies, and the regularization inherent to inversion procedures, all of which preferentially suppress small-scale structure and rapidly evolving perturbations, including the wavefronts of interest here.

Instead, we explore an alternative strategy that does not aim to reconstruct the full atmospheric state, but focuses on identifying the wavelengths in commonly observed photospheric lines at which the acoustic wavefront signal is most effectively captured. Using a numerical simulation, in which propagating wavefronts have already been identified, we perform spectral synthesis to determine the wavelengths at which wavefront-induced intensity fluctuations are maximum relative to background variability. Spectral response functions provide a natural quantitative framework for this analysis, as they describe how perturbations at different heights in the atmosphere map into wavelength-dependent intensity variations. Although acoustic waves are traditionally characterized through pressure perturbations in simulations and Doppler velocity measurements in observations, the detectability of these weak transient signals in spectra is primarily governed by the temperature sensitivity of a spectral line. Accordingly, our analysis focuses on temperature response functions, which directly quantify how depth-dependent thermal perturbations associated with the acoustic wavefronts translate into observable intensity variations. Doppler velocity is used only for wavefront identification and validation within the simulation, in which it is an easily accessible variable with a relatively large amplitude, while the observational strategy is optimized entirely in terms of intensity for which the response to velocity perturbations is much smaller than that to temperature fluctuations. By evaluating the response of the synthesized spectra to the height-dependent temperature fluctuations induced by a wavefront passage, we construct a detectability metric that quantifies the relative contributions of the wave signal and the background and identifies the spectral regions most favorable for wavefront detection using the successive-differencing technique.

Detection and characterization of local source wavefronts places stringent and often competing requirements on spatial resolution, temporal cadence, and spectral fidelity. Acoustic wavefronts associated with localized excitation events evolve on time scales of seconds, have spatial scales of tens of kilometers, and are most visible in the simulations as they propagate across a granule. Thus, observing them with spectroscopic raster-scanning is very likely not possible. Any sequential sampling in physical space mixes temporal evolution with spatial structure, effectively smearing or suppressing the signatures of interest. Integral-field spectroscopy or fast Fabry–Pérot-based spectral line scanning (at a limited number of wavelengths) is therefore preferred, as these preserve the instantaneous spatial coherence of the wavefront while retaining spectral sensitivity. In the latter case, finite time is required to switch between wavelengths; therefore, the image time series at different wavelengths, constructed by sequentially stepping through a limited set of line positions (and thus atmospheric heights), are not strictly co-temporal. We anticipate (and discuss further in Sections 2 and 3.4) that since the wavefront perturbations in which we are interested propagate upward in the atmosphere, this temporal offset can be accounted for, and used beneficially, in

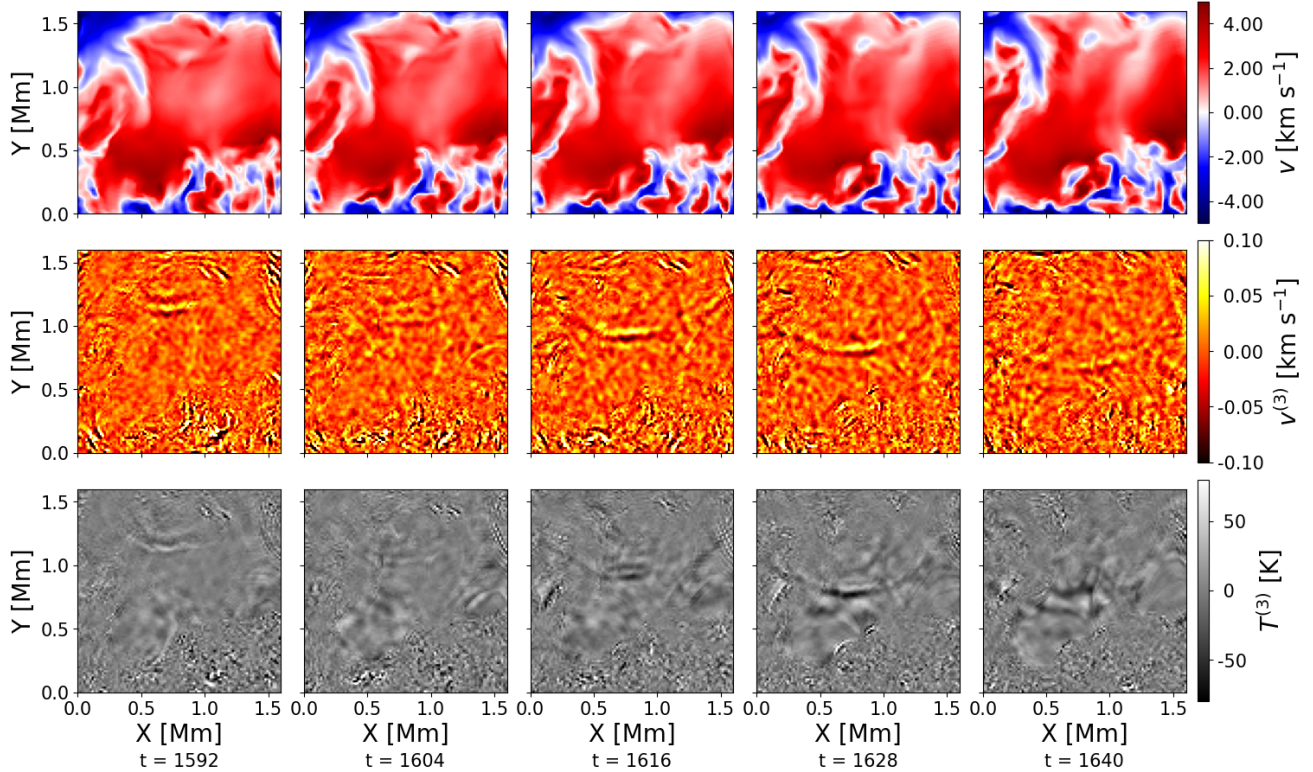


Figure 1. Propagation of a localized acoustic wavefront through the photosphere in a radiative MHD simulation. Panels show snapshots of the (A) line-of-sight velocity (*top*), its (B) third-order temporal difference (*middle*), and the corresponding (C) third-order temporal difference of temperature (*bottom*), revealing a coherent wavefront expanding across a granulation cell. Temporal differencing suppresses background convective motions and isolates the expanding wavefront as it traverses a granule, demonstrating the basis of the detection technique used throughout this work. Temporal increment between image frame is 12 s. The original MURaM data cubes (N_x, N_y, N_z) = (384, 384, 256) are cropped to a $100 \times 100 \times 100$ pixel sub-region (1.6 \times 1.6 Mm horizontally). The sub-region shown in this image is centered at pixel $(x_c, y_c) = (48, 119)$, where (x_c, y_c) denote global indices in the full MURaM cube.

observation and data analysis strategies (Section 4). Because of its combination of ultra-high spatial and spectral resolution, rapid cadence, and full-field spatial sampling, we suggest that the National Science Foundation’s Daniel K. Inouye Solar Telescope (DKIST, Rimmele et al., 2020) Visible Tunable Filter (VTF, Schmidt et al., 2016) is well positioned to meet the observational requirements of this problem (Section 4).

2 WAVEFRONT DETECTION

Our analysis is based on a MURaM small-scale dynamo radiative magnetohydrodynamic simulation of the upper solar convection zone, photosphere, and lower chromosphere (simulation O16b SSD in Rempel, 2014). The computational domain spans 6×6 Mm horizontally and 3 Mm vertically, with a grid spacing of 16 km and a cadence of 2 s. We examine in detail an acoustic wavefront that occurs in the period between 1584–1682 s MURaM time.

The spatial and temporal resolution of the simulation are sufficient to resolve propagating acoustic wavefronts produced by local sources. It is the same simulation that was used in the development of the wavefront detection techniques we employ (Bahauddin and Rast, 2021, 2023). The wavefront we analyze in

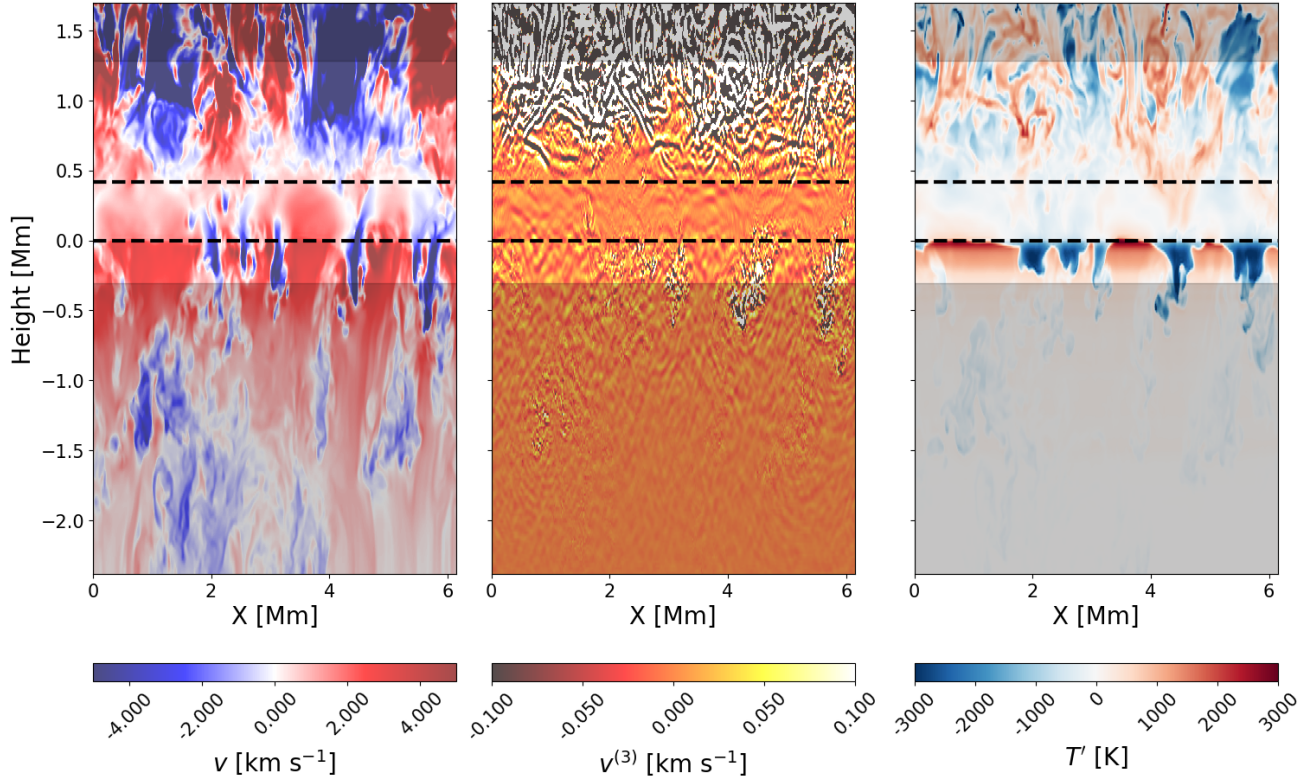


Figure 2. Height-dependent velocity and temperature structure of the simulated atmosphere at a single time step. The panel shows an instantaneous vertical slice of (A) **line-of-sight velocity** v (left), (B) **temporal velocity difference** $v^{(3)}$ (middle), and (C) **temperature fluctuations** $T' = T - T_0$, where T_0 is the horizontal mean temperature at each height (right), over the full vertical extent (3 Mm) of the MURaM solution. The *dashed black* fiducial lines indicate the most wave-sensitive height range, $z \sim 0.0 - 0.42$ Mm (discussed in Section 2), since the background atmosphere in this region is quietest. The *shaded gray* regions indicate the layers excluded during spectral synthesis (Section 3).

detail in this paper is shown in Figure 1 as it propagates through the photosphere. Of particular note is the visibility of the wavefront after application of a triple temporal difference filter to the Doppler velocity ($v^{(3)}$, *second row*) and temperature field ($T^{(3)}$, *bottom row*). Wavefronts identified in the MURaM simulation typically originate from shallow sources, located tens of kilometers beneath the photosphere. As they pass through the photosphere, their horizontal phase speeds are initially very high and decrease with time as they expand, to asymptotically approach the sound speed at the source depth (Bahauddin and Rast, 2023). Once identified in velocity difference images, the propagating wavefronts are often just barely visible without temporal differencing in animated time series of the raw Doppler or temperature perturbation maps.

However, the visibility of the wavefronts is not uniform with height in the simulated atmosphere because the amplitude of the wavefront relative to the background motions (which we consider here as noise) varies with height. Figure 2 illustrates the background motions in which the wavefronts are embedded, showing the vertical velocity (A), the vertical velocity temporal difference (B), and the temperature fluctuations about the horizontal mean (C), as functions of height at a single instant of time. The region of convective overshoot, here taken as $z \sim 0.0$ to 0.42 Mm above the photosphere (delimited with horizontal *black dashed* fiducial lines), has the lowest amplitude background noise. Convective amplitudes increase below the photosphere ($z \lesssim 0.0$), and the domain is filled with large amplitude acoustic gravity waves above $z \sim 0.42$. If the simulation accurately represents the Sun, observations aiming to uncover impulsively

generated wavefronts have the highest likelihood of success if they are focused on the solar convective overshoot region. Since the domain is quite shallow, the upper boundary condition may play some role in establishing the chromospheric wave field. However, a wave field of similar amplitude is also found in deeper simulations (those of Rempel, 2025) with an upper boundary that extends into the corona. The origin, persistence, and importance of this wavefield to chromospheric structure is being pursued.

3 SPECTRAL SIGNATURES

The first step in quantifying the spectral sensitivity to local wavefront perturbations is the synthesis of the emergent Stokes I intensity from the MURaM simulation. We synthesize three photospheric lines: Fe I 5250.2 Å, Fe I 5250.6 Å, and Fe I 6302.5 Å, over wavelength ranges 5249.90–5250.45 Å, 5250.45–5251.00 Å, and 6302.20–6302.90 Å with 0.005 Å sampling. We consider only vertical rays and restrict the vertical extent of the atmosphere to the *unshaded* region in Figure 2 ($-0.30 \leq z \leq 1.28$ Mm). The latter restriction reduces the computational cost of the transfer calculation while still capturing the full range of heights that contribute to absorption in the lines of interest. Using the temperature, pressure, and line-of-sight velocity profiles with height in a small region of interest (see Section 3.2 below), we synthesize emergent spectra for each atmospheric column. We employ the `SNAP` code (Milić and van Noort, 2018), solving the polarized radiative transfer equation assuming Local Thermodynamic Equilibrium (LTE). Thus, we obtain $I(\lambda, t)$ for each atmospheric column, at each horizontal location in the simulation.

3.1 Response

The sensitivity of the emergent intensity to atmospheric perturbations is quantified through the spectral response function. Of particular interest for wavefront detection is the temperature response function (RF_T), which measures the linear changes in the emergent intensity at a given frequency produced by localized perturbations in T as a function of perturbation height z . `SNAP` computes the derivatives of the specific intensity with respect to changes in T by evaluating variations in the formal solution that result from small perturbations to the atmospheric column at each height. The result is a two-dimensional kernel,

$$\text{RF}_T(\lambda, z) = \frac{\partial I(\lambda)}{\partial T(z)}, \quad (1)$$

for each atmospheric column at each time step in the simulation.

The response functions for the wavelength ranges we consider peak between $z \approx 0$ km and 500 km. Because the acoustic wavefronts in the simulation are most apparent as small amplitude fluctuations in the overshoot region, which lies within this height range, these response functions provide a natural bridge between the physical perturbations induced by the wavefront passage and its observational signatures.

3.2 Perturbation definition and wavefront mask

With the goal of determining where in the spectrum the acoustic wavefront will leave its largest signature, we first identify the location of the wavefront as a function of time in the simulation. We then find the wavelengths for which the signal from those locations in the atmosphere is largest compared to other background contributions (Section 3.3). This will motivate observation strategies that either fix on the most sensitive wavelengths or amplify the wave signature by tracking the wave in spectral space (Section 4).

To determine the locations at which the wavefront is most clearly defined against the background, we manually locate its position at each height as a function of time in the $v^{(3)}$ (velocity difference) images.

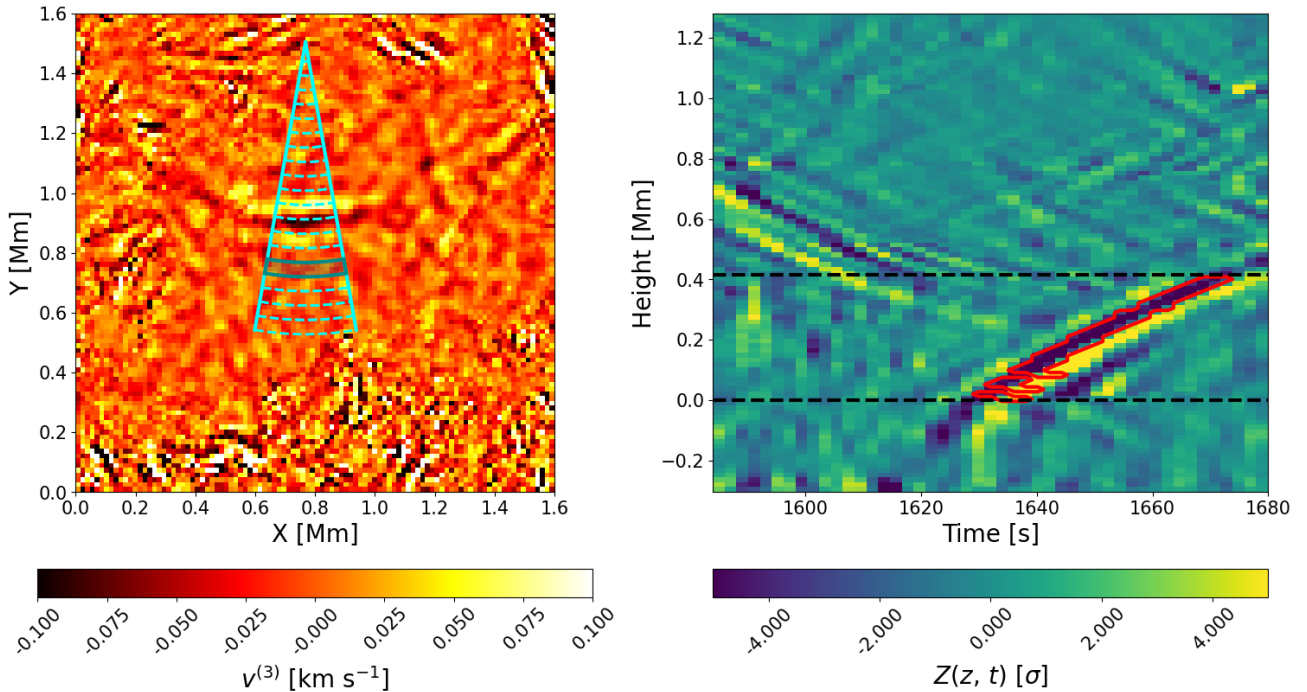


Figure 3. Construction of azimuthally averaged acoustic mask from the MURaM simulation. **(A)** **Temporal velocity difference** $v^{(3)}$ snapshot (*left*) showing the acoustic wavefront in the MURaM photosphere with concentric annuli around fitted center (*cyan*). Annulus selected for analysis indicated with dark, bolded boundaries. **(B)** **Standard score** $Z(z, t)$ **map** for the region of interest (*right*), revealing a clear, height-dependent acoustic propagation pattern. *Dashed black* lines indicate the most wave-sensitive height range while the *solid red* line outlines the region isolated by the mask described in Section 3.2.

We measure its angular extent and, by fitting circular arcs to its shape, locate the center of its expansion. Using these measurements, we define the region of wavefront propagation (the wedge in Figure 3A) and divide it into concentric annular segments with fixed radial widths of 3 pixels (48 km). Three pixels is the approximate radial extent of the wavefront in the direction of propagation in the simulations.

Focusing on temperature fluctuations (with similar analysis also done for Doppler velocity and pressure perturbations), we compute, at each height z and time t , the average temperature in each annulus in the wavefront region, $\bar{T}(r, z, t)$, where r labels the distance of the annulus from the center of expansion. Using this, we define perturbations as

$$\delta T(r, z, t) = \bar{T}(r, z, t) - \bar{T}_{\text{bg}}(r, z), \quad (2)$$

where \bar{T}_{bg} is the mean temperature in each annulus at each height averaged over a wave-free time interval (simulation time period 1504 – 1560 s, ending approximately 30 s before the wavefront is visible at any r in the photosphere). It is important to note that the temperature perturbation $\delta T(r, z, t)$ is defined relative to the mean quiet background state, and thus does not explicitly separate the wavefront contributions from others such as granulation. As the background thermodynamic structure evolves in time, $\delta T(r, z, t)$ does not represent a purely wave-isolated perturbation but the total deviation from the mean quiet reference atmosphere when the wave is present.

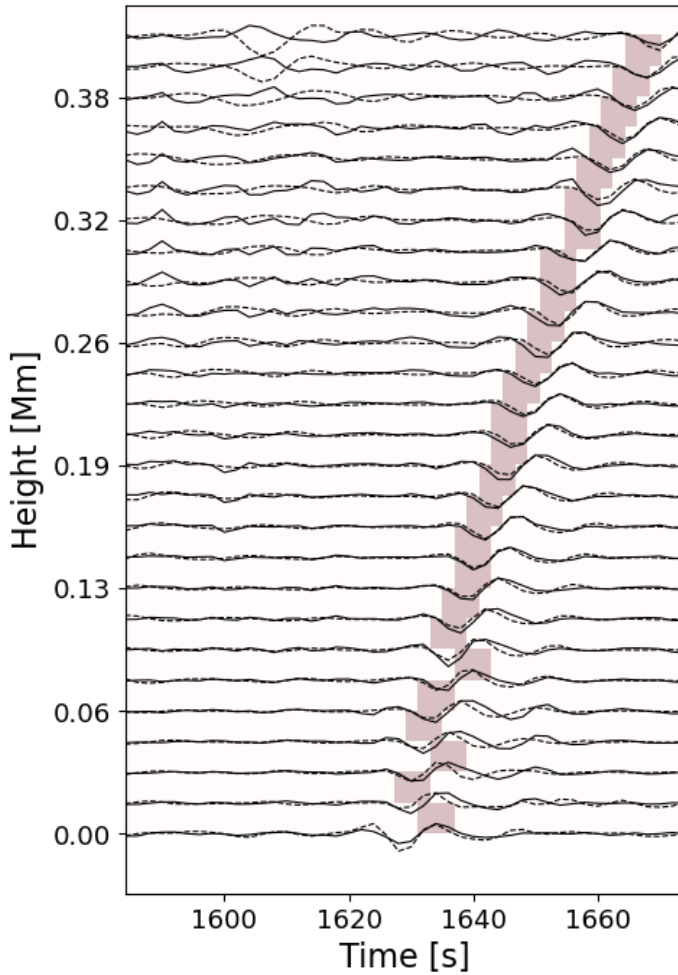


Figure 4. One-dimensional upward wave propagation constructed from azimuthally averaged perturbations in the annulus of interest. The temporally differenced velocity $v^{(3)}$ (solid black line) as well as differenced temperature $\delta T^{(3)}$ (dashed black line) are shown as functions of time and vertically offset by height, revealing the coherent upward progression of the acoustic wavefront through the atmosphere. The shaded red area indicates the wave mask M_{wave} of Section 3.2 used to isolate the wave-dominated portion of the signal.

To select the annulus with the strongest wave signal for further analysis, we compute the $v^{(3)}$ standard score (Z -score) for each annulus, and select the annulus with the strongest integrated Z -score over height and time. This annulus is highlighted with bolded boundaries in Figure 3A. While subsequent analysis focuses primarily on temperature perturbations and their influence on the emergent spectra, we defined this annular region of interest using $v^{(3)}$ because the acoustic wavefront shows the strongest signal in this variable. As illustrated by Figure 4, which plots the average $v^{(3)}$ and $\delta T^{(3)}$ in the annulus of interest as a function of time and height, and as expected for a non-oscillatory acoustic pulse, there is little phase difference between $v^{(3)}$ and $T^{(3)}$ (and thus the wave-induced velocity and temperature perturbations) as the wavefront propagates.

With the annulus of interest defined, a time-height map of the Z -score for that annulus can be used to isolate the wave perturbation. The upward propagating wavefront in this map (Figure 3B) is clearly visible in the convective overshoot region, corresponding to the region where $|Z| > 3$ between $0.0 \leq z \leq 0.42$

(bounded by horizontal fiducial lines in the plot). Thus, a mask $M_{\text{wave}}(z, t)$ that selects the time steps surrounding the Z -score peak at each height can be used to isolate the wavefront. We take one time-step either side of that peak (± 2 s) to define when the wave is present at each height because this approximates the time it takes for the acoustic perturbation to cross three radial grid cells (~ 48 km), which is about the thickness of the wavefront in the direction of propagation. This time-height mask is over-plotted with a *red* outline in Figure 3B and superimposed as a shaded region in Figure 4. Although the masked region looks like a trough in the difference variables, it physically corresponds to a region of positive (upward) velocity and positive temperature perturbation. With this mask, the wave temperature perturbations can be identified as

$$\delta T_{\text{wave}}(z, t) = \delta T(z, t) \cdot M_{\text{wave}}(z, t). \quad (3)$$

This is the characteristic temperature perturbation at the wave location as a function of height and time.

3.3 Sensitivity Measure

For small amplitude temperature perturbations, the change in emergent intensity at each horizontal location in the simulation at a given wavelength λ is approximately

$$\Delta I(\lambda, t) = \int \text{RF}_T(\lambda, z) \delta T(z, t) dz, \quad (4)$$

where contributions from velocity and pressure fluctuations are not included because their contributions to ΔI are negligible for the photospheric lines we are considering. With Equation 4, we can define a wavelength-dependent sensitivity measure $\text{SNR}(\lambda, t)$ to assess the wavelengths at which the wavefront signal exceeds most that due to typical background fluctuations. The wave-related contributions to the intensity changes $\Delta I(\lambda, t)$ are

$$\Delta I_{\text{wave}}(\lambda, t) = \int \text{RF}_T(\lambda, z) \delta T_{\text{wave}}(z, t) dz, \quad (5)$$

where the integral is effectively over the limited range of heights over which the wave is found due to the mask that has been applied to obtain δT_{wave} (Equation 3). The background noise contribution to $\Delta I(\lambda, t)$ can be expressed as

$$\Delta I_{\text{std}}(\lambda, t) = \int \text{RF}_T(\lambda, z) \sigma_T(z, t) dz, \quad (6)$$

where $\sigma_T(z, t)$ is the standard deviation of the temperature fluctuations at each height and the integral extends over all heights. We measure the standard deviation of the temperature fluctuations over the annulus of interest (Figure 3A) and all times over which the spectral synthesis was performed (1584–1682 s).

The wavefront sensitivity measure is then

$$\text{SNR}(\lambda, t) = \frac{\Delta I_{\text{wave}}(\lambda, t)}{\Delta I_{\text{std}}(\lambda, t)}, \quad (7)$$

and the wavelength of maximum sensitivity is

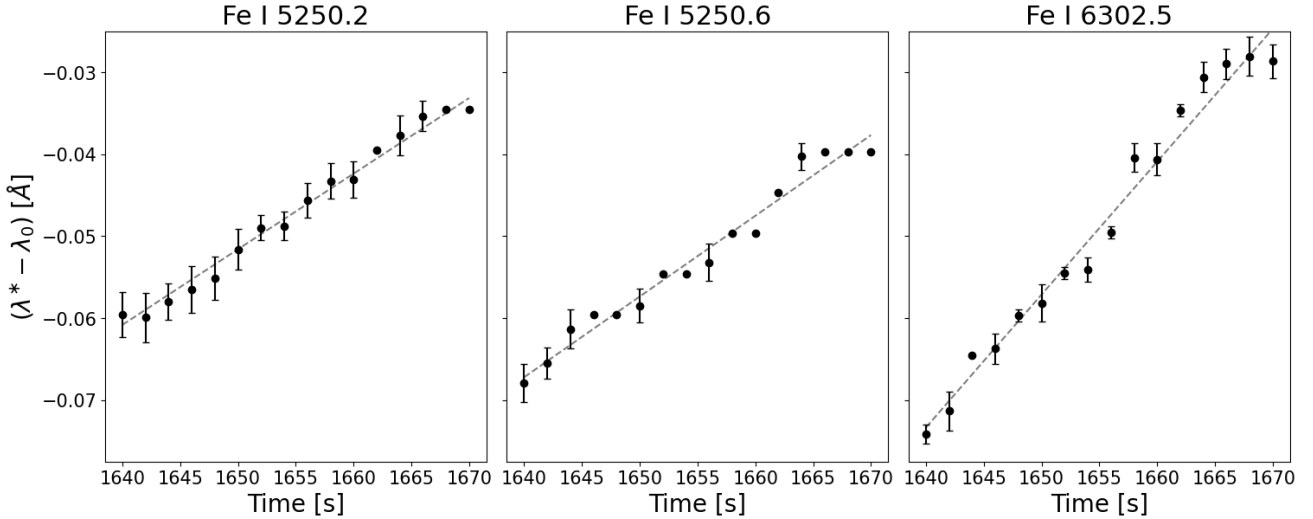


Figure 5. Time-dependent drift of the wavelength of maximum temperature sensitivity, λ^* , averaged over the annulus of interest. The evolution of λ^* toward the rest-frame line center (λ_0) traces the upward propagation of the acoustic wavefront and the corresponding shift in the atmospheric layer contributing most strongly to the intensity response. Error bars indicate the standard deviation of λ^* over pixels.

$$\lambda^*(t) = \arg \max_{\lambda} \text{SNR}(\lambda, t) . \quad (8)$$

As with the response function (Equation 1), the wavefront sensitivity measure (Equation 7), and thus $\lambda^*(t)$, is computed independently for each pixel in the annulus of interest. The average $\lambda^*(t)$, over that annulus, is plotted as function of time in Figure 5, and represents the wavelength at which the characteristic signal from the wavefront has the largest amplitude compared to variations at that wavelength due to fluctuations at all heights.

We define a second quantity of interest λ^{**} , the spatial average (over the annulus of interest) of the wavelength at which the sensitivity measure is highest at any time. For each spatial pixel within the annulus of interest, we find the wavelength at which the wave sensitivity reaches its global maximum when considering all wavelengths and all times within the wave mask. We report a single λ^{**} for each spectral line by spatially averaging this quantity, yielding the wavelength at which the wavefront is, on average, most detectable. The distribution of wavelength values contributing to this mean (the individual pixel values) is shown in Figure 6. The values found for λ^{**} and their standard deviations are $\lambda^{**} = 5250.148 \text{ \AA}$, 5250.583 \AA , 6302.425 \AA , and $\sigma_{\lambda^{**}} = 0.0031 \text{ \AA}$, 0.0028 \AA , 0.0046 \AA for the Fe I 5250.2, Fe I 5250.6, and Fe I 6302.5 lines respectively. For all three lines, the maximum sensitivity occurs at $t = 1642 \text{ s}$. This time corresponds to a wavefront height between $z = 0.128$ and 0.176 Mm above the photosphere (above the mean $\tau = 1$ height in the simulation).

3.4 Wavefront signatures

As the wave propagates upward, the wavelength of maximum sensitivity $\lambda^*(t)$ drifts to longer wavelengths with time for all the lines examined (Figure 5). For all of the lines, the maximum spectral sensitivity occurs on the blue (shorter wavelength) side of the line. This is due to the systematic Doppler distortion of the lines caused by the granular upflow underlying the region of wavefront propagation. As shown in Figure 6,

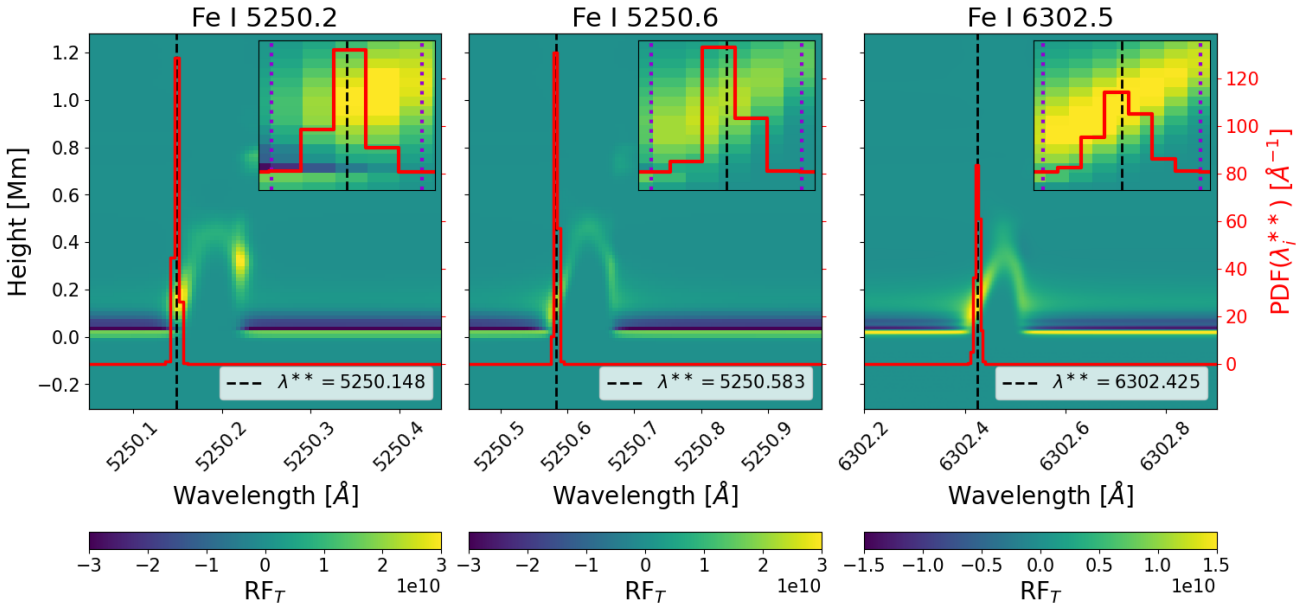


Figure 6. The average, over the annulus of interest, of the temperature response function RF_T for each atmosphere making up the annulus of interest at $t = 1640$ s, across the Fe I 5250.2, 5250.6, and 6302.5 spectral lines (*background*). The probability density function of λ^{**} for each pixel in the annulus of interest is over-plotted in red, with λ^{**} indicated with a *black* vertical line. The insets zoom into the λ^{**} region and indicate the VTF spectral element extent with *dotted* vertical lines.

the Doppler distortion of the line decreases the slope of the height of the response function peak with wavelength. With the decreased slope, a narrower range of heights contributes to the response at any given wavelength on the short wavelength side of the spectral line than on its right, increasing the sensitivity measure that we have defined. In general, line profiles with less steep wings are preferred when localizing observations in height.

Because maximum spectral sensitivity occurs on the short wavelength side of the line, the wavelength of maximum sensitivity shifts to longer wavelengths (towards the line core) as the wavefront propagates upward in the atmosphere; the location of the wavefront perturbation, captured by the mask, moves higher in the atmosphere with time (Figure 3B) so that wavelength of maximum sensitivity moves toward the line core. The rate of this systematic shift does not simply reflect the wavefront propagation speed. Instead, $\lambda^*(t)$ is determined by the atmosphere through which the wave is traveling (defining the response function), the vertical propagation speed of the wavefront, and the spectral slope of the line wing. It can be used in the development of a robust observing strategy (Section 4), either by fitting $\lambda^*(t)$ for each spectral line using the simulation or, more satisfactorily, by determining from first principles how λ^* evolves given the spectral line and the atmosphere of interest. The latter is the focus of future efforts. Here we measure the slopes and find them to be 9.223×10^{-4} , 9.845×10^{-4} , and 1.621×10^{-3} $\text{\AA}/\text{s}$ for Fe I 5250.2, Fe I 5250.6, and Fe I 6302.5 respectively.

4 OBSERVATIONAL STRATEGIES – IMPLICATIONS FOR DKIST/VTF

The two measures, $\lambda^*(t)$ and λ^{**} motivate different observing strategies. The first is an estimate for the best wavelength sequence to employ to follow the wavefront propagation, while the second is an estimate of the best overall choice of wavelength at which to perform monochromatic imaging at high cadence.

Observing at λ^{**} is roughly equivalent to observing the wavefronts as they propagate horizontally at the height of maximum sensitivity. Observing sequentially over the wavelengths $\lambda^*(t)$, on the other hand, allows collection of a cube of data that can be post-processed to find the signatures of wavefronts as they propagate upward with height, measuring, in order, at the most sensitive wavelength at each height. For a more robust measurement, the individual λ^* maps in multi-wavelength observations could be shifted in time, stacked, and summed to obtain the mean signal over all heights. In this operation, the wave signal adds coherently, while the variation in granulation with height contributes to some cancellation of the background and consequent enhancement of the propagating wavefront signal-to-noise.

The VTF provides full-field imaging spectroscopy across 5200–8700 Å, with a $60'' \times 60''$ field of view sampled at $0.014''$ per pixel, corresponding to about 10.5 km on the solar surface. This sampling is comparable to the 16 km horizontal grid spacing of the MURaM simulation analyzed for this paper, and allows access to the spatial scales over which acoustic wavefronts remain coherent and may be recoverable by temporal differencing (Bahauddin and Rast, 2023). The spectral resolving power of the VTF is $R \sim 10^5$ (e.g., ~ 0.06 Å resolution with ~ 0.03 Å sampling near 6000 Å) over a free spectral range of ~ 10 Å. In detail, the VTF spectral sampling width is about 0.023 Å at 5250 Å and 0.033 Å at 6302 Å (Tritschler et al., 2016; Schmidt et al., 2016). These band passes are over-plotted in the insets of Figure 6.

As discussed above, the distributions of λ^{**} , as determined from the individual atmospheres of the annulus of interest, have widths of $\sigma_{\lambda^{**}} = 0.0031$ Å, $\sigma_{\lambda^{**}} = 0.0028$ Å, and $\sigma_{\lambda^{**}} = 0.0046$ Å for Fe I 5250.2, Fe I 5250.6, and Fe I 6302.5, respectively. Thus, the range of λ^{**} values found for each of these lines lies well within one spectral sampling element of the VTF. VTF observations centered on λ^{**} or λ^* will capture a relatively broad range of wavelengths and consequently sample a range of atmospheric heights. From Figure 6, it is clear that, in the case of Fe I 5250.2 for example, centering the VTF passband on λ^{**} will include significant contributions from the continuum. Those contributions are dominated by granulation noise that will likely overpower the wave signal in monochromatic observations. More generally, the range of atmospheric heights encompassed by the VTF bandpass may smear the wave signal. However, the blue wing of Fe I 5250.6, and even more so that of Fe I 6302.5, are shallower and thus less contaminated by contributions away from the wavelength of maximum sensitivity (see insets of Figure 6). Here we focus our observational plans on the Fe I 6302.5 line, though careful convolution with both VTF spectral bandpass and the DKIST point spread function (PSF) is required to fully assess the potential of each line for local wavefront discovery.

4.1 Monochromatic Observations

To comply with the requirements of the temporal difference filter, the cadence of the monochromatic observations should be at or below the critical sampling rate $\Delta t = \Delta x/v_{\text{ph}}$, where Δx is the spatial sampling width and v_{ph} is the phase speed of the wavefront. The phase speed of the wavefront at $z = 0.152$ Mm, the midpoint of the Fe I 6302.5 λ^{**} height, is 10.5 km/s. Critical sampling of the wavefront thus occurs at a cadence of 1 s. The practical viability of this cadence is governed by the signal-to-noise requirements based on the intensity fluctuations caused by acoustic perturbations.

For intensity-based diagnostics, the relevant signal-to-noise ratio is defined as

$$\text{SNR} \equiv \frac{I}{\sigma_I}, \quad (9)$$

where I is the measured intensity and σ_I is the corresponding uncertainty. Detecting a fractional intensity perturbation $\Delta I/I$ with N_σ significance requires

$$\text{SNR} \gtrsim \frac{N_\sigma}{\Delta I/I}. \quad (10)$$

In practice, this implies the following order-of-magnitude requirements: a 1% intensity fluctuation requires $\text{SNR} \sim 100$ for marginal (1σ) detectability and ~ 300 for robust (3σ) detection; a 0.5% fluctuation requires $\text{SNR} \sim 200\text{--}600$; and a 0.1% fluctuation requires $\text{SNR} \sim 300$ for marginal detection and 1000 for robust detection.

Quantitative guidance on the achievable cadence vs. signal-to-noise trade space is assessed by the VTF Instrument Performance Calculator (IPC, National Solar Observatory, 2026). For monochromatic (single-wavelength) intensity imaging, the IPC indicates that an SNR of 235 can be achieved at a cadence of 0.04 s, while relaxing the cadence to 1.04 s increases the SNR to 1200. While our analysis is for a single representative wavefront, the phase speed of the wavefront depends on the depth of the excitation source, with deeper sources producing higher phase speeds. Because the source depth in the solar atmosphere is not known a priori, and constraining it is one of the primary goals of the observations we propose, the cadence must accommodate a plausible range of propagation speeds. For wavefront perturbation speeds between 7 km/s, corresponding to the lower bound of the photospheric sound speed, and 11 km/s, the upper range observed in the simulations analyzed here, sampling intervals of between 1.5 and 0.95 s satisfy the critical sampling requirement. Therefore, we suggest monochromatic sampling at λ^{**} with a cadence of 0.5 s, which over-samples the expected wavefront propagation while maintaining a high SNR of approximately 817. Post-processing can further increase the effective SNR through temporal averaging (e.g., a running average).

4.2 Multi-wavelength Observing Strategy

For multi-wavelength observations, the goal is to scan the range of wavelengths $\lambda^*(t)$ that track the upward propagation of the wavefront through the atmosphere. The wavelengths chosen must span a significant portion of that range of $\lambda^*(t)$ and follow the slope of λ^* with time (Figure 5). The scan across all wavelengths must be completed quickly enough to allow repeat measurements at any single wavelength with a cadence that allows temporal differencing of the time series. To accomplish this without knowledge of the wavefront location, a data volume in (x, y, λ, t) must be assembled from which the trajectories can be extracted.

The wavelength of maximum sensitivity $\lambda^*(t)$ in the blue shoulder of Fe I 6302.5 (in Figure 5) extends from 6302.419 Å and 6302.465 Å as the wavefront propagates upward in the atmosphere over a time period of 30 s, with a slope of 1.621×10^{-3} Å/s. The VTF IPC imposes a minimum wavelength step between successive observations of 0.0315 Å. Observations sampling $\lambda^*(t)$ would ideally be spaced closer in wavelength, but under this restriction, the strategy is to interleave observations over three wavelengths, $\lambda^*(t)$ and $\lambda^{**} \pm 0.0315$. The wavelengths to observe are then 6302.3935, 6302.425, and 6302.4565 Å. This can be done with a cadence of 0.48 s achieving a signal to noise at each wavelength of 408. Since the endpoints of this wavelength triplet lie slightly outside of the $\lambda^*(t)$ range, and thus have lower wavefront sensitivity, an alternative two wavelength option is warranted, observing the lower end of the $\lambda^*(t)$ range at 6302.42 Å and 6302.45 Å. This two-wavelength observation can be done with a cadence of 0.48 s with a signal to noise of 527. The propagation of the wavefront between these two wavelengths takes about 18.5 s.

An observation period of 60 s with excellent seeing would allow approximately two full wave periods to be sampled under the first multiwavelength scheme and approximately three under the second. Longer excellent seeing time series would be even more beneficial. In the MURaM photosphere, we observe about 50 propagating wavefront events per hour over the 36 Mm^2 field. Over the full $60'' \times 60''$ VTF field of view we thus expect to observe about 40 events per minute.

As discussed above, post observational analysis of the multi wavelength data cube is critical and should focus on using the height-time dependencies of wavefront trajectories to increase detection likelihood. This can be done by looking directly for propagating signals in the four dimensional space-wavelength-time data cube or by shifting the data accumulated at different wavelengths and times so that they can be added together to reinforce the signal. Since the data is to be acquired at a cadence of 0.48 s and the propagation time across the sampled wavelengths takes about 15 to 30 s for the two observation scenarios, trajectories with different upward signal propagation speeds should be accessible and distinguishable in the data cube.

5 CONCLUSIONS

In this work, we have developed a physically motivated framework for detecting locally excited wavefronts in the solar photosphere by connecting the source wavefronts to their wavelength-dependent observational signatures in commonly observed Fe I spectral lines. This connection was established by determining the wavelengths of maximum sensitivity to the wavefront perturbation as it propagates upward into the overshoot region of a simulated solar atmosphere. Based on these synthetic results we defined two observation strategies for the detection of these transient events.

While the detailed results derived are based on a single representative acoustic source, our preliminary examination on more than 25 acoustic events indicates that the qualitative behavior reported here, particularly the speed and extent of wavefront propagation, is common across many of these sources. A comprehensive ensemble analysis spanning the full source population is currently in progress and will be presented in future work.

A central conclusion of the work is that the measurement techniques we suggest are well fit to DKIST/VTF capabilities, though a smaller minimum wavelength separation between successive observations would be very beneficial. While the detection of expanding, spatially coherent wavefronts is incompatible with raster-based spectroscopy, which entangles spatial structure with temporal evolution and thus confuses signals from fast transient events, the VTF's Fabry-Pérot-based, full-field imaging spectroscopy preserves their coherence. Moreover the temporal offset between time-series of interleaved wavelengths, can be leveraged to enhance the propagating signal. The VTF performance calculations suggest that, under the VTF operational constraints, sparse wavelength sampling concentrated in the most sensitive line-wing regions can satisfy the temporal requirements imposed by signal propagation, while still retaining sufficient spectral information to track the upward evolution implied by the drift of the optimal sensitivity wavelength.

At the same time, the approach carries inherent limitations that arise directly from its design. First, the usability of the wavefront identification technique depends sensitively on the stability and alignment of successive image frames. Wavefront identification is based on detecting coherent, rapidly evolving perturbations against the more slowly varying background, such that small residual differences between consecutive frames can produce a difference signal. Although post-image reconstruction can help, it cannot remove image misalignment and instability entirely and therefore these effects impose practical limits on the minimum detectable wave amplitude.

Second, the requirement for sub-second to second temporal cadence, necessary to robustly uncover the wavefront signal from the noise by temporal differencing, constrains the number of wavelength positions that can be sampled within a single scan. Consequently, the method trades spectral coverage for temporal sampling. This, combined with practical restrictions on the minimum wavelength separation between successive observations, limits the ability to perform detailed atmospheric inversions or to disentangle overlapping contributions from different heights.

Third, spectral resolution and stability play a central role in determining the vertical localization of the measurement. Our current method relies on isolating wave-induced perturbations over a narrow and stable wavelength range, as encoded in the wavelength-dependent response functions of the spectral line. If the instrument resolution or stability worsens, contributions from a wider range of atmospheric heights are mixed within a single wavelength sample, reducing the contrast of the wavefront signal relative to background fluctuations. In this regard, spectral lines with soft (not steep) shoulder more reliably localize measurements in height.

Despite these limitations, our assessment indicates that the DKIST 4 m aperture, in combination with the VTF Fabry–Pérot imager, constitutes one of the few observational platforms capable of simultaneously satisfying the spatial, spectral, and temporal resolution constraints required by the method developed here. Consequently, local acoustic wavefront detection represents both a compelling scientific objective and a stringent benchmark for DKIST’s ability to probe weak, rapidly evolving photospheric dynamics at their intrinsic spatial and temporal scales. Successful application of the framework developed here would transform a long-standing problem into an observationally accessible diagnostic.

CONFLICT OF INTEREST STATEMENT

The authors declare that the research was conducted in the absence of any commercial or financial relationships that could be construed as a potential conflict of interest.

AUTHOR CONTRIBUTIONS

CM: Conceptualization, Formal analysis, Methodology, Visualization, Writing – original draft; MR: Conceptualization, Interpretation, Methodology, Supervision, Writing – original draft; SB: Conceptualization – original project conception, Methodology, Writing – original draft; IM: Software, Writing – review & editing.

FUNDING

This work was partially supported by the National Science Foundation (NSF) Award No. 2206589. CM acknowledges support from the University of Colorado Hale Fellowship program and the NSF Graduate Research Fellowship Program (GRFP), Grant No. DGE-2040434.

ACKNOWLEDGMENTS

Sincere thanks to M. Rempel for his continued and ongoing scientific generosity. The simulation material is based upon work supported by the NSF National Center for Atmospheric Research, which is a major facility sponsored by the U.S. National Science Foundation under Cooperative Agreement No. 1852977.

MATERIALS AND METHODS

The analysis presented in this study is based on a three-dimensional radiative magnetohydrodynamic simulation of quiet-Sun convection produced with the MURaM code, spanning the upper convection zone, photosphere, and lower chromosphere. Localized acoustic wavefronts are identified using a temporal differencing technique applied to the simulated velocity and temperature fields, followed by azimuthal averaging to isolate coherent wave-induced perturbations from background convective variability. Synthetic spectral profiles are computed using the SNAPI radiative transfer framework, and temperature response functions are used to quantify the wavelength-dependent sensitivity of spectroscopic intensity to wave-driven thermal perturbations. All subsequent detectability metrics are derived from these response functions and annulus-averaged perturbations, enabling direct assessment of optimal spectral sampling strategies for DKIST/VTF observations.

DATA AVAILABILITY STATEMENT

The simulation data and analysis products supporting the findings of this study are available from the corresponding author upon request. The numerical simulation was produced using the MURaM code, and all post-processing, spectral synthesis, and analysis procedures were carried out using SNAPI code and custom python script described in the text. Derived data products and scripts necessary to reproduce the figures and results can be provided by the corresponding author.

REFERENCES

Aerts, C., Christensen-Dalsgaard, J., and Kurtz, D. W. (2010). *Asteroseismology* (Springer, Dordrecht)

Ambastha, A., Basu, S., and Antia, H. M. (2003). Flare-Induced Excitation of Solar p modes. *Sol. Phys.* 218, 151–172. doi:10.1023/B:SOLA.0000013043.45512.20

Bahauddin, S. M., Fischer, C. E., Rast, M. P., Milic, I., Woeger, F., Rempel, M., et al. (2024). Observations of Locally Excited Waves in the Low Solar Atmosphere Using the Daniel K. Inouye Solar Telescope. *Astrophys. J. Lett.* 971, L1. doi:10.3847/2041-8213/ad62f8

Bahauddin, S. M. and Rast, M. P. (2021). Identifying Acoustic Wave Sources on the Sun. I. Two-dimensional Waves in a Simulated Photosphere. *Astrophys. J.* 915, 36. doi:10.3847/1538-4357/abfdae

Bahauddin, S. M. and Rast, M. P. (2023). Identifying Acoustic Wave Sources on the Sun. II. Improved Filter Techniques for Source Wavefield Seismology. *Astrophys. J.* 955, 31. doi:10.3847/1538-4357/aced46

Balmforth, N. J. (1992). Solar pulsational stability - III. Acoustical excitation by turbulent convection. *Mon. Not. R. Astron. Soc.* 255, 639. doi:10.1093/mnras/255.4.639

Bello González, N., Franz, M., Martínez Pillet, V., Bonet, J. A., Solanki, S. K., del Toro Iniesta, J. C., et al. (2010). Detection of Large Acoustic Energy Flux in the Solar Atmosphere. *Astrophys. J. Lett.* 723, L134–L138. doi:10.1088/2041-8205/723/2/L134

Christensen-Dalsgaard, J. (2002). Helioseismology. *Reviews of Modern Physics* 74, 1073–1129. doi:10.1103/RevModPhys.74.1073

Cox, A. N. (2002). Unsolved Problems in Stellar Pulsation Physics (invited review). In *IAU Colloq. 185: Radial and Nonradial Pulsations as Probes of Stellar Physics*, eds. C. Aerts, T. R. Bedding, and J. Christensen-Dalsgaard. vol. 259 of *Astronomical Society of the Pacific Conference Series*, 21

Daszyńska-Daszkiewicz, J. (2015). Energetic properties of stellar pulsations across the Hertzsprung-Russell diagram. In *European Physical Journal Web of Conferences*. vol. 101 of *European Physical Journal Web of Conferences*, 01002. doi:10.1051/epjconf/201510101002

Del Toro Iniesta, J. C. and Ruiz Cobo, B. (1996). Stokes Profiles Inversion Techniques. *Sol. Phys.* 164, 169–182. doi:10.1007/BF00146631

del Toro Iniesta, J. C. and Ruiz Cobo, B. (2016). Inversion of the radiative transfer equation for polarized light. *Living Reviews in Solar Physics* 13, 4. doi:10.1007/s41116-016-0005-2

Donea, A. C. and Lindsey, C. (2005). Seismic Emission from the Solar Flares of 2003 October 28 and 29. *Astrophys. J.* 630, 1168–1183. doi:10.1086/432155

Goldreich, P. and Keeley, D. A. (1977). Solar seismology. II. The stochastic excitation of the solar p-modes by turbulent convection. *Astrophys. J.* 212, 243–251. doi:10.1086/155043

Goldreich, P. and Kumar, P. (1990). Wave Generation by Turbulent Convection. *Astrophys. J.* 363, 694. doi:10.1086/169376

Goldreich, P., Murray, N., and Kumar, P. (1994). Excitation of Solar p-Modes. *Astrophys. J.* 424, 466. doi:10.1086/173904

Goode, P. R., Strous, L. H., Rimmele, T. R., and Stebbins, R. T. (1998). On the Origin of Solar Oscillations. *Astrophys. J. Lett.* 495, L27–L30. doi:10.1086/311203

Hansen, S. C., Cally, P. S., and Donea, A.-C. (2016). On mode conversion, reflection, and transmission of magnetoacoustic waves from above in an isothermal stratified atmosphere. *Mon. Not. R. Astron. Soc.* 456, 1826–1836. doi:10.1093/mnras/stv2770

Kitiashvili, I. N., Kosovichev, A. G., Mansour, N. N., Wray, A. A., and Sandstrom, T. A. (2019). The Origin of Deep Acoustic Sources Associated with Solar Magnetic Structures. *Astrophys. J.* 872, 34. doi:10.3847/1538-4357/aafac1

Kosovichev, A. G. and Zharkova, V. V. (1998). X-ray flare sparks quake inside Sun. *Nature* 393, 317–318. doi:10.1038/30629

Lighthill, M. J. (1952). On Sound Generated Aerodynamically. I. General Theory. *Proceedings of the Royal Society of London Series A* 211, 564–587. doi:10.1098/rspa.1952.0060

Lighthill, M. J. (1954). On Sound Generated Aerodynamically. II. Turbulence as a Source of Sound. *Proceedings of the Royal Society of London Series A* 222, 1–32. doi:10.1098/rspa.1954.0049

Lindsey, C., Buitrago-Casas, J. C., Martínez Oliveros, J. C., Braun, D., Martínez, A. D., Ortega, V. Q., et al. (2020). Submerged Sources of Transient Acoustic Emission from Solar Flares. *Astrophys. J. Lett.* 901, L9. doi:10.3847/2041-8213/abad2a

Lindsey, C. and Donea, A.-C. (2013). Statistics of Local Seismic Emission from the Solar Granulation. In *Journal of Physics Conference Series*. vol. 440 of *Journal of Physics Conference Series*, 012044. doi:10.1088/1742-6596/440/1/012044

Lindsey, C., Donea, A. C., Martínez Oliveros, J. C., and Hudson, H. S. (2014). The Role of Magnetic Fields in Transient Seismic Emission Driven by Atmospheric Heating in Flares. *Sol. Phys.* 289, 1457–1469. doi:10.1007/s11207-013-0389-2

Lindsey, C. and Rempel, M. (2020). Using the Butterfly Effect to Probe How the Sun Generates Acoustic Noise. *Sol. Phys.* 295, 26. doi:10.1007/s11207-020-1580-x

Martínez, A. D., Ortega, V. Q., Buitrago-Casas, J. C., Martínez Oliveros, J. C., Calvo-Mozo, B., and Lindsey, C. (2020). Ultra-impulsive Solar Flare Seismology. *Astrophys. J. Lett.* 895, L19. doi:10.3847/2041-8213/ab9173

Milić, I. and van Noort, M. (2018). Spectropolarimetric NLTE inversion code SNAPI. *Astron. Astrophys.* 617, A24. doi:10.1051/0004-6361/201833382

[Dataset] National Solar Observatory (2026). Visible Tunable Filter, version 3.4. <https://nso.edu/telescopes/dkist/instruments/vtf/>. Accessed: 2026-01-15

Nigam, R., Kosovichev, A. G., Scherrer, P. H., and Schou, J. (1998). Asymmetry in Velocity and Intensity Helioseismic Spectra: A Solution to a Long-standing Puzzle. *Astrophys. J. Lett.* 495, L115–L118. doi:10.1086/311219

Nordlund, A. and Stein, R. F. (1998). The excitation and damping of p-modes. In *New Eyes to See Inside the Sun and Stars*, eds. F.-L. Deubner, J. Christensen-Dalsgaard, and D. Kurtz. vol. 185, 199

Philedit, J., Belkacem, K., Samadi, R., Barban, C., and Ludwig, H. G. (2020). Modelling the asymmetries of the Sun's radial p-mode line profiles. *Astron. Astrophys.* 635, A81. doi:10.1051/0004-6361/201936847

Rast, M. P. (1995). On the Nature of “Exploding” Granules and Granule Fragmentation. *Astrophys. J.* 443, 863. doi:10.1086/175576

Rast, M. P. (1997). Photospheric Downflows: How deep, how coherent, how important? In *SCORe'96 : Solar Convection and Oscillations and their Relationship*, eds. F. P. Pijpers, J. Christensen-Dalsgaard, and C. S. Rosenthal. vol. 225, 135–138. doi:10.1007/978-94-011-5167-2-13

Rast, M. P. (1999). The Thermal Starting Plume as an Acoustic Source. *Astrophys. J.* 524, 462–468. doi:10.1086/307782

Rast, M. P., Nordlund, A., Stein, R. F., and Toomre, J. (1993). Ionization Effects in Three-dimensional Solar Granulation Simulations. *Astrophys. J. Lett.* 408, L53. doi:10.1086/186829

Rempel, M. (2014). Numerical Simulations of Quiet Sun Magnetism: On the Contribution from a Small-scale Dynamo. *Astrophys. J.* 789, 132. doi:10.1088/0004-637X/789/2/132

[Dataset] Rempel, M. (2025). Private communication

Rimmele, T. R., Goode, P. R., Harold, E., and Stebbins, R. T. (1995). Dark Lanes in Granulation and the Excitation of Solar Oscillations. *Astrophys. J. Lett.* 444, L119. doi:10.1086/187874

Rimmele, T. R., Warner, M., Keil, S. L., Goode, P. R., Knölker, M., Kuhn, J. R., et al. (2020). The Daniel K. Inouye Solar Telescope - Observatory Overview. *Sol. Phys.* 295, 172. doi:10.1007/s11207-020-01736-7

Roth, M., Franz, M., Bello González, N., Martínez Pillet, V., Bonet, J. A., Gandorfer, A., et al. (2010). Surface Waves in Solar Granulation Observed with SUNRISE. *Astrophys. J. Lett.* 723, L175–L179. doi:10.1088/2041-8205/723/2/L175

Roxburgh, I. W. and Vorontsov, S. V. (1997). On the formation of spectral line profiles of solar P modes. *Mon. Not. R. Astron. Soc.* 292, L33–L36. doi:10.1093/mnras/292.1.L33

Samadi, R., Belkacem, K., and Sonoi, T. (2015). Stellar oscillations - ii - the non-adiabatic case. *EAS Publications Series* 73-74, 111–191. doi:10.1051/eas/1573003

Samadi, R. and Goupil, M. J. (2001). Excitation of stellar p-modes by turbulent convection. I. Theoretical formulation. *Astron. Astrophys.* 370, 136–146. doi:10.1051/0004-6361:20010212

Samadi, R., Goupil, M. J., and Lebreton, Y. (2001). Excitation of stellar p-modes by turbulent convection. II. The Sun. *Astron. Astrophys.* 370, 147–156. doi:10.1051/0004-6361:20010213

Schmidt, W., Schubert, M., Ellwarth, M., Baumgartner, J., Bell, A., Fischer, A., et al. (2016). End-to-end simulations of the visible tunable filter for the Daniel K. Inouye Solar Telescope. In *Ground-based and Airborne Instrumentation for Astronomy VI*, eds. C. J. Evans, L. Simard, and H. Takami. vol. 9908 of *Society of Photo-Optical Instrumentation Engineers (SPIE) Conference Series*, 99084N. doi:10.1117/12.2232518

Severino, G., Magrì, M., Oliviero, M., Straus, T., and Jefferies, S. M. (2001). The Solar Intensity-Velocity Cross Spectrum: A Powerful Diagnostic for Helioseismology. *Astrophys. J.* 561, 444–449. doi:10.1086/323243

Skartlien, R. and Rast, M. P. (2000). p-Mode Intensity-Velocity Phase Differences and Convective Sources. *Astrophys. J.* 535, 464–472. doi:10.1086/308845

Skartlien, R., Stein, R. F., and Nordlund, Å. (2000). Excitation of Chromospheric Wave Transients by Collapsing Granules. *Astrophys. J.* 541, 468–488. doi:10.1086/309414

Stein, R. F. (1967). Generation of Acoustic and Gravity Waves by Turbulence in an Isothermal Stratified Atmosphere. *Sol. Phys.* 2, 385–432. doi:10.1007/BF00146490

Stein, R. F. and Nordlund, Å. (1991). Convection and Its Influence on Oscillations. In *Challenges to Theories of the Structure of Moderate-Mass Stars*, eds. D. Gough and J. Toomre. vol. 388, 195. doi:10.1007/3-540-54420-8_67

Strous, L. H., Goode, P. R., and Rimmele, T. R. (2000). The Dynamics of the Excitation of Solar Oscillations. *Astrophys. J.* 535, 1000–1013. doi:10.1086/308892

Tritschler, A., Rimmele, T. R., Berukoff, S., Casini, R., Kuhn, J. R., Lin, H., et al. (2016). Daniel K. Inouye Solar Telescope: High-resolution observing of the dynamic Sun. *Astronomische Nachrichten* 337, 1064. doi:10.1002/asna.201612434